IEEE Access
Multidisciplinary | Rapid Review | Open Access Journal

Received 20 October 2023, accepted 2 November 2023, date of publication 6 November 2023, date of current version 9 November 2023.

Digital Object Identifier 10.1109/ACCESS.2023.3330215

RESEARCH ARTICLE

Research on Full Brake-By-Wire System and Clamping Force Estimation Strategy Based on Redundant Drive Motors

LIANG CHU, PENGH ZHU, AND CHENG CHANG
College of Automotive Engineering, Jilin University, Changchun 130011, China

Corresponding author: Cheng Chang (changcheng3170@163.com)

This work was supported by the Tianjin Science and Technology Program under Grant 20YFZCGX00770.

ABSTRACT In this study, a full brake-by-wire system with a dual-drive motor as a redundant power source and a planetary roller screw (PRSM) as a motion conversion mechanism is proposed for automated driving and wire-controlled chassis. Its parameters are matched, and the prototype is trial-produced. Aiming at the proposed full brake-by-wire system, a clamping force estimation control strategy is proposed that comprehensively considers electric caliper dynamics, stiffness, and friction models. In particular, considering the influence of motor temperature on the output torque, a temperature estimation model based on the proximal policy optimization-reinforcement learning (PPO-RL) algorithm was proposed, which was proven to effectively predict the motor temperature with an average error of only 1.06%. Finally, a hardware-in-the-loop test was performed, and the experimental results verified the effectiveness and superiority of the proposed system and control strategy, with a fast response, good clamping force continuous-following effect, and high clamping force estimation accuracy.

INDEX TERMS Full brake-by-wire system, redundant drive motors, motor temperature estimation, PPO-RL algorithm, clamping force estimation.

I. INTRODUCTION

According to the ''Energy-saving and New Energy Vehicle Technology Roadmap 2.0'' released by the Chinese Society of Automotive Engineering in October 2020, China's automotive industry will be transformed into an electrified industry by 2035, and intelligent internet-connected vehicles will run widely in China, with broad prospects for the development of highly automated driving vehicles.

Currently, autonomous vehicle technology is generally divided into six levels from L0 to L5, where L3 represents the transition between low-level driving assistance and advanced autonomous driving development. The L3 level and above autonomous driving also put forward higher requirements for the chassis system, which requires layout flexibility, architectural compatibility, and control integration [1].

The wire-controlled chassis system decouples the mechanical connection between the driver operating mechanism and the actuators of the chassis subsystems, and controls the chassis execution action through electrical signals, which has the characteristics of a faster response, more accurate following, and more stable control. Moreover, its integrated control is the centralized embodiment of vehicle dynamics in all motion dimensions, with all-round, multilevel, and strong coupling characteristics, and it is the best platform to meet the performance requirements of the L3 level and above the automated driving system.

Therefore, automated driving and wire-controlled chassis are complementary, mutually reinforcing relationships.

The brake-by-wire system is one of the key subsystems of a wire-controlled chassis. Depending on their structural characteristics and working principles, they mainly include electrohydraulic brakes (EHB) and electromechanical brakes (EMB) [2], [3]. The EHB system cancels the vacuum booster and realizes brake booster and active braking functions

The associate editor coordinating the review of this manuscript and approving it for publication was Geng-Ming Jiang.

through a motor-driven brake master cylinder piston. The brake pedal can be decoupled from the brake master cylinder to a certain extent but still retains the hydraulic line; therefore, there is a risk of brake fluid leakage [4], [5]. Compared with hydraulic brakes, the EMB system completely eliminates hydraulic lines and decouples the mechanical connection between the brake pedal and the braking system. Therefore, the EMB system is a fully brake-by-wire system [6], [7].

Based on the power transmission method of EMB systems, known mechanical structures can be classified into three types [8], [9]. The first is the lever/wedge self-increasing force type, which produces a self-increasing force effect through a wedge or lever structure [10]. These advantages include low motor power requirements and a high braking efficiency. The disadvantages include the extremely high mechanical performance requirements of the wedge and roller, assembly difficulties, high heat generation in the drivetrain, and high cost [11], [12]. The second type is an electromagnetic clutch that uses a two-stage planetary gear system. The two stages of the planetary gear system are equipped with two electromagnetic clutches. When power is applied, the friction disk and clutch fit together and transmit the motor driving force [13], [14]. When the power was turned off, the friction disk and clutch separated, and the clamping state of the brake disc was maintained. The structure does not require the motor to remain stuck for a long time, and the motor is automatically disengaged when the power is turned off; therefore, it requires less motor performance [15], [16]. However, because the motor must drive the friction disc, the rotational inertia is high. The friction disc must be periodically replaced to ensure power transmission [17], [18]. A low supply voltage results in a decrease in the suction capacity of the electromagnetic clutch. The third type is the planetary gear + ball screw type, which is powered by a brushless DC motor or a permanent magnet synchronous motor [19], [20]. The angular velocity of the motor was reduced and the motor torque was amplified using a planetary gear mechanism. Finally, through the ball-screw mechanism, the rotary motion is converted into a linear motion, and the piston is pushed to achieve displacement [21], [22]. The structure is highly integrated, with high maturity and low cost, but it is more difficult to assemble [23], [24].

In summary, the third type is the most widely used and lowest-overall cost technical solution for passenger cars [16], [25]. Moreover, it ensures that the advanced automatic driving vehicle can still actively brake when a single-point failure occurs in the brake-by-wire system [26]. Simultaneously, to achieve smaller axial dimensions and a higher load capacity, an EMB structure with dual drive motors as the redundant power source and planetary gears and planetary roller screws as the drive mechanism based on the third type is proposed in this paper [27].

Clamping-force estimation methods include sensor-based clamping-force estimation and sensorless clamping-force estimation. For the sensor-based clamping force estimation method, the force sensor must be able to withstand high temperatures if it is close to the friction plate, and if it is far away from the friction plate, the hysteresis effect of the electric caliper can lead to inaccurate force measurements. Additionally, the sensor must be calibrated separately, which presents a disadvantage in terms of cost and use [28], [29]. Therefore, sensorless clamp-force estimation has gradually become a research hotspot. Currently, sensorless clamp force estimation strategies mainly include an estimation strategy based on the motor angle and an estimation strategy based on the motor current, both of which regard the electric caliper working process as a whole to carry out clamp force estimation [30], [31]. In fact, the performance of electric calipers in different stages of clamping force application, clamping force continuous climbing, and clamping force release are different; therefore, the above strategies cannot maintain a good accuracy of the clamping force estimation in all stages [32]. Therefore, it is necessary to propose a clamping force estimation strategy to adapt to different electric caliper operation stages. Meanwhile, the increase in motor temperature during the clamping force climbing process will have a certain effect on the motor output torque, thus reducing the accuracy of the clamping force estimation. Therefore, it is very important to consider the compensation of the motor temperature on the estimated clamping force [33].

For the proposed redundant drive motor EMB structure, and considering the effect of temperature on the motor output torque, a control strategy for clamping force estimation without sensors based on the proximal policy optimization-reinforcement learning (PPO-RL) algorithm temperature estimation model modification was proposed [34], [35].

The remainder of this paper is organized as follows. Section II illustrates the mechanical structure of the redundant drive motor EMB system, modeling of key components, and parameter matching. The electric caliper model and parameter identification of the proposed EMB system are described in Section III. Section IV proposes a motor temperature estimation model based on the PPO-RL algorithm to correct the motor output torque. The algorithm for clamping force estimation without sensors and hardware-in-the-loop test verification are presented in Section V. Section VI summarizes the article and addresses the directions for future work.

II. EMB SYSTEM STRUCTURE, KEY COMPONENT MODELING AND PARAMETER MATCHING

A. REDUNDANT DRIVE MOTOR EMB STRUCTURE

The EMB system structure investigated in this paper is shown in Fig. 1.

Where a. brushless DC drives motor 1, b. brushless DC drives motor 2, c. motor-locking mechanism, d. planetary gear transmission mechanism, e. spline, f. planetary roller screw, g. wheel cylinder piston, h. brake disc, and i. friction pad.

Working Principle: Brushless DC drive motor 1 and brushless DC drive motor 2 are redundant power sources for the

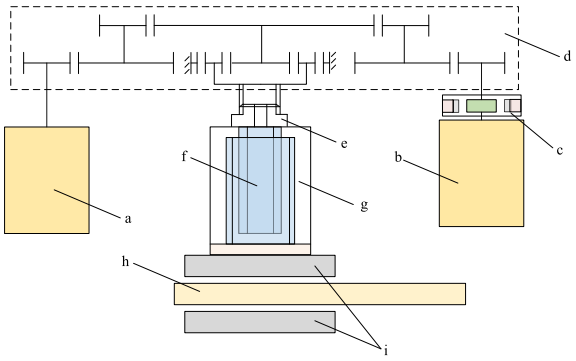

FIGURE 1. EMB system structure schematic.

actuator. The motor torque was transmitted to the PRSM through a planetary gear mechanism and spline. The PRSM is built into a wheel cylinder piston and pushes it in a linear motion. This brings the friction pad into contact with the brake disc, creating a clamping force perpendicular to it.

B. PLANETARY ROLLER SCREW MODELING

The PRSM is a transmission component that converts rotary motion into linear motion with the combined characteristics of threaded and rolling helical transmissions. Compared with ball screws, the threaded roller instead of the ball enables the load to be released quickly through many contact points, thus allowing a higher load and impact resistance. A typical nut movement-type PRSM explosion structure diagram is shown in Fig. 2.

The proposed EMB system uses a standard PRSM, in which the screw has only circular motion, the nut has only axial motion, and the roller has both rotation and revolution. The rotation of the screw drives the movement of the roller, and finally, the nut pushes the piston of the wheel cylinder to achieve a linear reciprocating motion, that is, to achieve the application and release of the caliper. A principle diagram of the movement of the standard PRSM is shown in Fig. 3.

The circular motion of the nut is constrained, the contact point A is the absolute instantaneous center of velocity, and the common angular velocity of the roller has the following relationship:

$$\omega_P = \frac{d_S}{2d_P}\omega_S = \frac{d_S}{2(d_S + d_R)}\omega_S \tag{1}$$

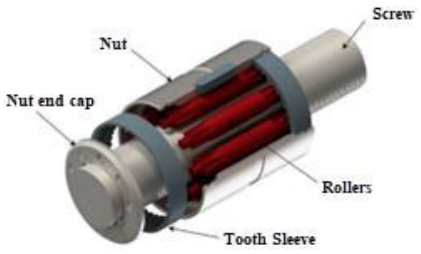

FIGURE 2. A typical PRSM structure exploded diagram.

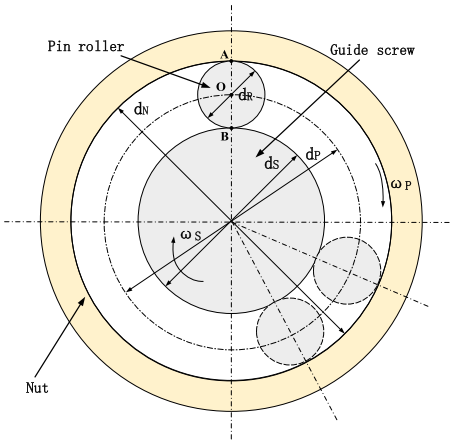

FIGURE 3. The movement principle diagram of the standard PRSM .

where ω_P is the roller revolution angular velocity; ω_S is screw angular velocity; d_P is roller revolution circle diameter; d_S is screw pitch diameter, d_R is roller pitch diameter, respectively.

The ratio of screw and roller pitch diameter k_m is:

$$k_m = \frac{d_S}{d_R} \tag{2}$$

Equation (1) can be expressed as:

$$\omega_P = \frac{k_m}{2(k_m + 1)}\omega_S \tag{3}$$

The integral form of (3) is given by:

$$\varphi_P = \frac{k_m}{2(k_m + 1)}\varphi_S \tag{4}$$

where φ_P is roller revolution rotation angle;

φ_S is screw rotation angle.

The planetary carrier rotation angle of the planetary gear $\theta_{carrier}$ is equal to φ_S:

$$\varphi_S = \theta_{carrier} \tag{5}$$

Assuming that the roller is in a pure rolling state, the arc length of roller rotation is equal to the arc length rolled over the nut.

$$\frac{\varphi_R d_R}{2} = \frac{\varphi_P d_N}{2} \tag{6}$$

where φ_R is the roller rotation angle; d_N is nut pitch diameter.

So,

$$\frac{\varphi_R}{\varphi_P} = \frac{d_N}{d_R} = \frac{d_S + 2d_R}{d_R} = k_m + 2 \tag{7}$$

Substituting (5) and (7) into (4):

$$\varphi_R = \frac{k_m(k_m + 2)}{2(k_m + 1)}\theta_{carrier} \tag{8}$$

For the standard PRSM, there is no axial relative displacement between the roller and nut, and the relative displacement between the roller and screw is the axial displacement of nut ξ_N. Therefore, the axial displacement of the nut can

be calculated in two ways: one is calculated by the roller rotation angle and by the roller revolution rotation angle. The calculation formula is as follows:.

$$\xi_N = \frac{\varphi_R}{2\pi}P = \frac{k_m(k_m+2)}{4\pi(k_m+1)}P \cdot \theta_{carrier} \tag{9}$$

$$\xi_N = \frac{\varphi_P}{2\pi}n_N P = \frac{k_m}{4\pi(k_m+1)}n_N \cdot P \cdot \theta_{carrier} \tag{10}$$

where P is roller pitch, n_N is heads number of nut threads.

The planetary carrier output torque of planetary gear $T_{carrier}$ is equal to the screw drive torque T_S of the PRSM.

$$T_S = T_{carrier} \tag{11}$$

The force transfer relationship of the PRSM is essentially the same as that of the screw and sleeve mechanisms. Therefore, the relationship between the nut thrust F_N and the screw drive torque T_S can be established by the following equation:

$$F_N = T_s\Theta_{prsm}\eta_{prsm} \tag{12}$$

$$\Theta_{prsm} = \frac{2k \cdot \tan\alpha_R}{d_S} \tag{13}$$

where F_N is the nut thrust, Θ_{prsm} is the torque transmission parameter of the PRSM, η_{prsm} is the transmission efficiency of the PRSM, k is the number of rollers, α_R is the lift angle of the roller thread.

C. MODELING OF PLANETARY GEAR REDUCTION MECHANISM

A structural sketch of the planetary gear train is shown in Fig. 4. The red shaft is the power input shaft, and the green shaft is the power output shaft. The two side gear transmissions are symmetrical to each other: the first-stage gear transmission ratio is i_{g1}, second-stage gear transmission ratio is i_{g2}, and planetary gear transmission ratio is i_{pg}.

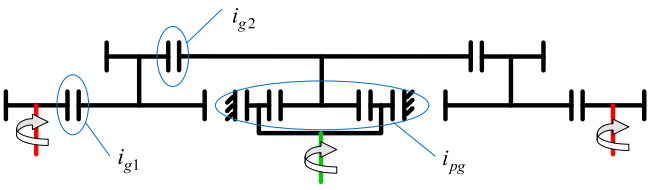

FIGURE 4. The structure sketch of planetary gear train.

The two-stage gear rotation ratio equations are as follows:

$$i_{g1} = \frac{z_2}{z_1} \tag{14}$$

$$i_{g2} = \frac{z_4}{z_3} \tag{15}$$

where z_1 denotes the motor gear tooth number, z_2 the first-stage lower gear tooth number, z_3 the first-stage higher gear tooth number, z_4 the second-stage higher gear tooth number. The expression of the planetary gear ratio is:

$$i_{pg} = 1 + \frac{z_r}{z_s} \tag{16}$$

where z_r is the gear ring tooth number and z_s is the sun wheel tooth number. The total transmission ratio of the single-side gear is:

$$i_g = i_{g1}i_{g2}i_{pg} = \frac{z_2z_4}{z_1z_3}(1+\frac{z_r}{z_s}) \tag{17}$$

Assuming that T_{e1} and T_{e2} are the output torques of brushless DC drive motors 1 and 2, respectively, $T_{carrier}$ is the output torque of the planetary gear. The relationship between the output torque and input torque of the planetary gear train is given by

$$T_{carrier} = (T_{e1} + T_{e2})i_g\eta_g \tag{18}$$

When the motor is not stuck, the rotation angle of the planetary frame and motor satisfy the following relationship:

$$\theta_{carrier} = \frac{Max(\theta_{M1}, \theta_{M2})}{i_g} \tag{19}$$

where θ_{M1} and θ_{M2} are the rotation angles of Motors 1 and 2, respectively.

D. MODELING OF BRUSHLESS DC DRIVE MOTOR

According to (12) and (18), the maximum drive-torque requirement for a single motor is.

$$T_{e\_\max} = \frac{F_{N\_\max}}{2i_g\eta_g\Theta_{prsm}\eta_{prsm}} \tag{20}$$

According to (10) and (19), the relationship between the motor angular velocity and translational velocity of the roller screw nut is given by

$$\dot{\xi}_N = \frac{k_m}{4\pi i_g(k_m+1)}n_N \cdot P \cdot \dot{\theta}_M \tag{21}$$

The output torques of both motors were eventually coupled to the sun wheel of the planetary gear train. Therefore, the speeds of both motors are the same, and are denoted as $\dot{\theta}_M$.

E. PARAMETER MATCHING

The parameters of the key components can be matched based on the structural scheme of EMB. The basic parameters of the target vehicle and its braking system are listed in Table 1. The parameter-matching process for the key components is shown in Fig. 5.

The selected motor model, planetary roller screw angular displacement transmission ratio, and total gear train transmission ratio are presented in Table 2. The parameters of the selected brushless DC motor are listed in Table 3, gear parameters of the selected planetary gear train are listed in Table 4, and selection parameters of the planetary roller screw are listed in Table 5.

A physical diagram of each component after matching the key parameters of the electric caliper prototype is shown in Fig. 6.

TABLE 1. The basic parameters of the target vehicle.

Parameters	Value	Unit
Wheel rolling radius	344	mm
Mass (unloaded/full load)	2015/2410	kg
centroid height	635/616	mm
Distance from centroid to front axle	1404/1562	mm
Front/Rear wheelbase	1650/1630	mm
axle wheelbase	2815	mm
Windward area	2.3	m^2
Wind resistance coefficient	0.3	--
Friction plate friction coefficient	0.38	--
Front/Rear brake disc effective radius	130/138	mm
Front/Rear wheel cylinder diameter	60/40	mm
Front/Rear brake disc thickness	28/10	mm

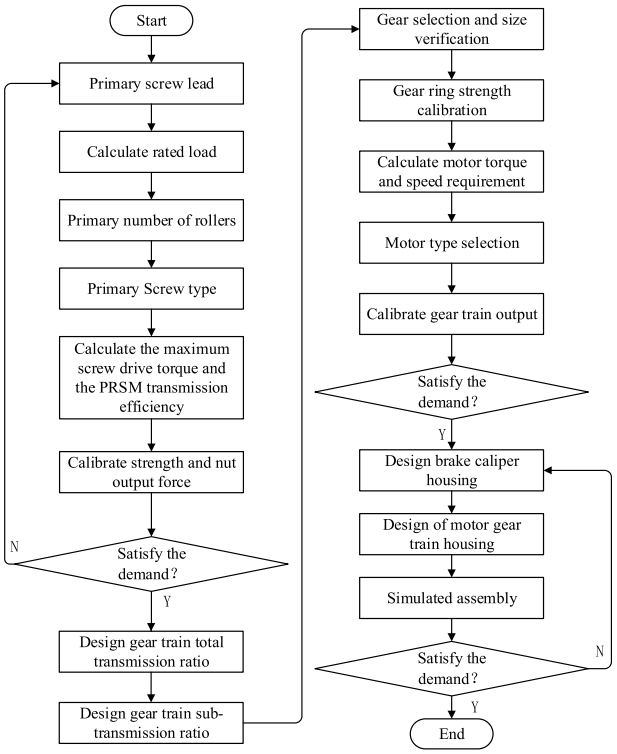

FIGURE 5. The parameter matching process of key components.

TABLE 2. Electric caliper key parameters.

Parameters	Value	Unit
BLDC motor type	48BLF02	--
Planetary roller screw angular displacement transmission ratio	0.5702	mm/rad
Total gear ratio	28	--

III. EMB PERFORMANCE MODELING AND PARAMETER IDENTIFICATION

A. REDUNDANT DRIVE ELECTRIC CALIPER DYNAMICS EQUATION

The electric caliper dynamics model for single motor operation is proposed:

$$J_1\ddot{\theta}_{M1} = T_{e1} - T_{f1} - T_L \tag{22}$$

TABLE 3. BLDC motor key parameters.

Parameters	Value	Unit
Motor rated voltage	12	V
Motor rated power	150	W
Motor peak current	40	A
Motor maximum power point torque	0.38	Nm
Motor peak speed	3000	r/min
Phase number	3	--
Motor pole pair number	5	--
Number of Hall sensors	3	Switch type

TABLE 4. Planetary gear train key parameters.

Parameters	Value	Unit
Motor gear tooth number	18	--
First stage lower gear tooth number	42	--
First stage higher gear tooth number	32	--
Second stage higher gear tooth number	83	--
Gear ring tooth number	51	--
sun wheel tooth number	12	--
Planetary gear tooth number	19	--

TABLE 5. PRSM key parameters.

Parameters	Value	Unit
Screw pitch diameter	28	mm
Roller revolution circle diameter	35	mm
Roller pitch diameter	7	mm
Nut pitch diameter	42	mm
Number of rollers	10	--
Total screw travel	50	mm
Number of threaded heads	6	--

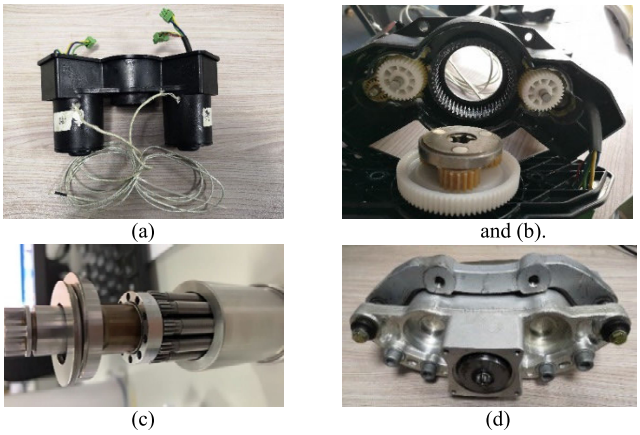

FIGURE 6. The physical diagram of each component. (a) Motor gear mechanism assembly. (b) Planetary gear train. (c) Planetary Roller Screw. (d) Electric caliper body.

Electric caliper dynamics model for simultaneous operation of dual motor:

$$J_2(\ddot{\theta}_{M1} + \ddot{\theta}_{M2}) = T_{e1} + T_{e2} - T_{f2} - T_L \tag{23}$$

where J_1 and J_2 are the system equivalent rotational inertia of the single-motor and dual-motor operations, respectively; $\ddot{\theta}_{M1}$ and $\ddot{\theta}_{M2}$ are the angular accelerations of motors 1 and 2, respectively; T_{f1} and T_{f2} are the system equivalent friction torques of the single motor and dual-motor operations, respectively; T_L is the system load, which directly reflects the electric caliper clamping force. The relationship between load and clamping force is as follows:

$$F_N = \frac{T_L \eta_g \eta_{prsm}}{H} \tag{24}$$

$$H = \frac{k_m(k_m+2)}{4\pi(k_m+1)} \frac{P}{i_g} \tag{25}$$

where H is the system equivalent transmission ratio, that is, the transmission coefficient of the motor rotation angle and the electric caliper piston displacement.

The dynamics model will output the demand system load for clamping force control.

B. SYSTEM EQUIVALENT ROTATIONAL INERTIA

Using the system energy equivalence principle, the equivalent rotational inertia of the system was calculated for the single- and dual-motor operations.

When a single motor runs, the inoperative motor must be superimposed on the rotational inertia of the system as a load. The equivalent rotational inertia of the system is.

$$J_1 = 2J_M + J_{Gear} + \frac{J_S}{i_g^2} + \frac{m_{Nut} d_{Nut}^2}{4} \tag{26}$$

where J_M is the motor rotational inertia, J_{Gear} is the equivalent rotational inertia of the planetary gear train, J_S is the PRSM rotational inertia, m_{Nut} is the PRSM nut mass, d_{Nut} is the effective diameter of the PRSM nut.

When a single motor runs, J_{Gear} is calculated as follows:

$$J_{Gear} = \frac{J_{g1}}{i_{g1}^2} + \frac{J_{Sun}}{(i_{g1} i_{g2})^2} + \frac{3J_P}{(i_P i_{g1} i_{g2})^2} + \frac{J_C}{i_g^2} + \frac{J_{g2}}{i_{g1}^2} \tag{27}$$

where J_{g1} and J_{g2} are the rotational inertias of motor 1 and motor 2 drive gears, respectively; J_{Sun} is the rotational inertia of the sun wheel; J_P is the rotational inertia of the planetary wheel; J_C is the rotational inertia of the planetary frame; i_P is the ratio of the planetary gear to the sun wheel.

Because the drive gear structure is the same, it can be considered that $J_{g1} = J_{g2}$ and (27) can be simplified as follows:

$$J_{Gear} = \frac{2J_{g1}}{i_{g1}^2} + \frac{J_{Sun}}{(i_{g1} i_{g2})^2} + \frac{3J_P}{(i_P i_{g1} i_{g2})^2} + \frac{J_C}{i_g^2} \tag{28}$$

When the dual motor runs, there is no non-working motor load and the equivalent rotational inertia of the system is.

$$J_2 = J_M + J_{Gear} + \frac{J_S}{i_g^2} + \frac{m_{Nut} d_{Nut}^2}{4} \tag{29}$$

C. ELECTRIC CALIPER STIFFNESS MODEL

An electric caliper stiffness model was used to climb and decay the clamping force. In the climbing phase, the model can be used for the first clamping force build-up. For the decay phase, the model can be used to control the position of friction plate release.

The climbing and decay of the clamping force were local nonlinear curves with respect to time. An electric caliper stiffness model based on total actuator deformation is expressed as follows:

$$\begin{cases} F_N = 0 (x_e \le 0) \\ F_N = K_1 x_e + b_1 (0 < x_e < x_0) \\ F_N = K_4 x_e^3 + K_3 x_e^2 + K_2 x_e + b_2 (x_e \ge x_0) \end{cases} \tag{30}$$

$$x_e = x - x_{ag} \tag{31}$$

where $K_1 \sim K_4$, b_1, b_2, and x_0 are the parameters to be identified; x_e is the total deformation of the electric caliper; x is the electric caliper piston displacement; x_{ag} is the brake disc clearance.

The control variable in the above equation is the total deformation x_e. However, x_e cannot be measured in practical engineering, and the key position parameter x_0 is a dynamic value that is difficult to identify, resulting in poor system robustness.

Therefore, we cancel the key position identification parameter x_0, replace the unmeasurable total deformation x_e with the relative motor Hall phase angle $\Delta\sigma_{Hall}$, and consider the contact state bit of the electric caliper friction pad and brake disc as the origin of the independent variable. An electric caliper stiffness model based on the relative motor Hall phase angle was proposed. For the clamping force-climbing phase, the model formula is as follows:

$$\begin{cases} F_N = 0 \ (u_0 \le u \le u_2) \\ F_N = A_0 + A_1 \cdot \cos(W \cdot \Delta\sigma_{Hall}) \\ \quad + B_1 \cdot \sin(W \cdot \Delta\sigma_{Hall}) \ (u_2 < u \le u_3) \end{cases} \tag{32}$$

where is the motor Hall phase angle, σ_{Hall} is the cumulative change in the Hall sensor in motor 1 or motor 2, the relative motor Hall phase angle $\Delta\sigma_{Hall}$ is the relative cumulative change with the initial cumulative change removed, A_0, A_1, B_1, and W are the parameters to be identified, u is the electric caliper piston real-time position, u_0 is the end position of the electric caliper completely released, u_2 is the friction pad and brake disc contact moment position, u_3 is the position after the first clamping is completed.

For the clamping force decaying phase, the model formula is described as:

$$\begin{cases} F_N = 0 \ (u_0 \le u \le u_2) \\ F_N = A \cdot e \wedge (-((\Delta\sigma_{Hall} - B)/C)^2) - D \ (u_2 < u \le u_3) \end{cases} \tag{33}$$

where, A, B, C, and D are identification parameters.

The stiffness model parameters were identified using an electric caliper prototype; the fitted curves are shown in Fig.7.

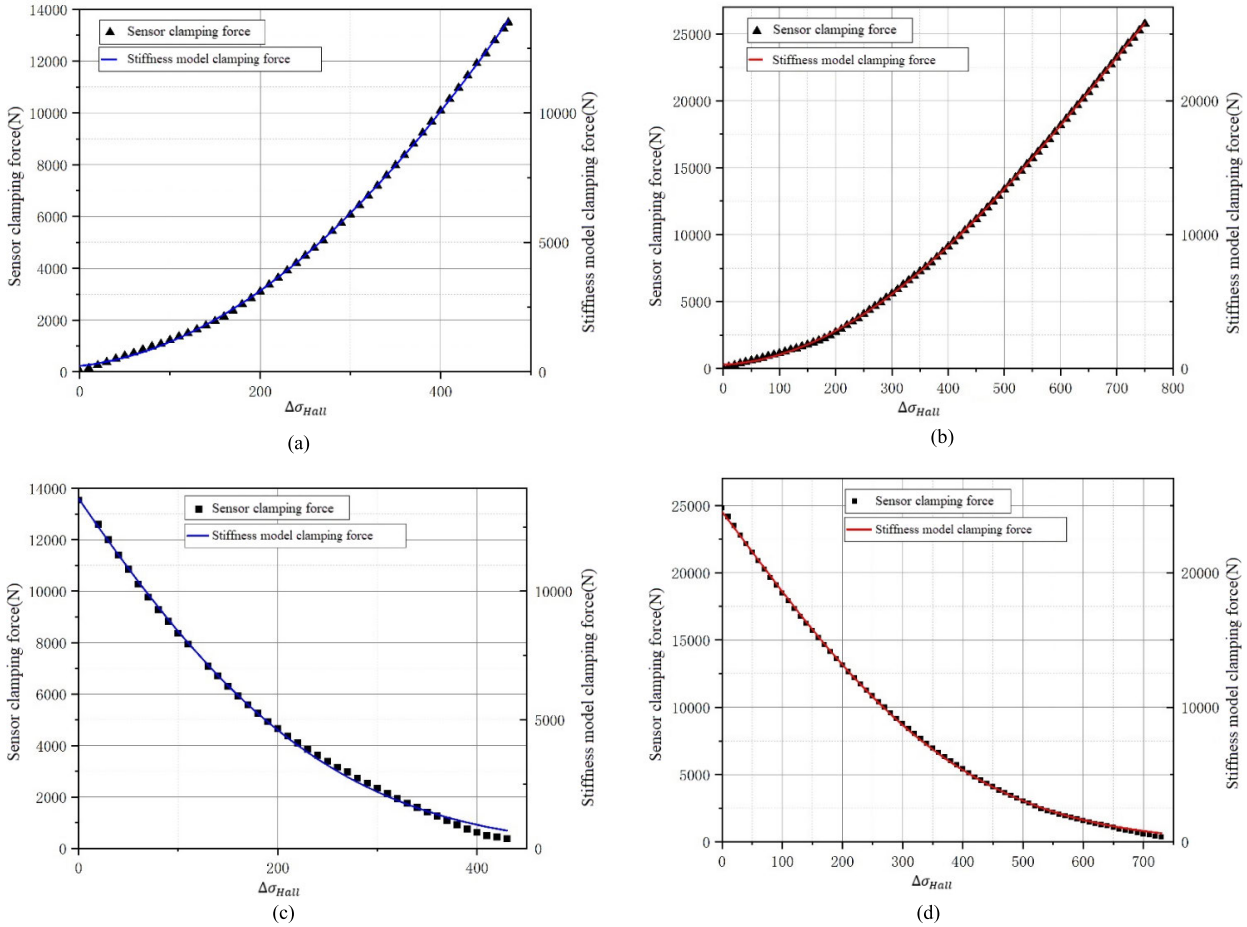

FIGURE 7. The Electric caliper stiffness model fitting curves. (a) Single motor clamping force climbing stage. (b) Dual motor clamping force climbing stage. (c) Single motor clamping force decay stage. (d) Dual motor clamping force decay stage.

The key parameters of the electric caliper stiffness model after the parameter identification are listed in Table 6.

TABLE 6. The electric caliper stiffness model key parameters.

Parameters	Value: Single motor	Value: Dual motor
A_0	48950	25500
A_1	-48420	-24920
B_1	2614	1062
W	0.001491	0.00207
A	26010	37020
B	-314.8	-342.1
C	391	533.1
D	0	0

D. ELECTRIC CALIPER FRICTION MODEL

An electric caliper may require frequent adjustments to the clamping force after the completion of the first clamping. The electric caliper was operated in a low-speed and high-torque state. The relationship between the system friction torque and the angular velocity was described using a friction model.

In this study, we considered the static friction, Coulomb friction, viscous friction, and Stribeck friction models to establish a friction model for an electric caliper. The basic equations of the proposed friction model are as follows.

$$T_f(\omega) = \begin{cases} T_{fe} & \text{if } \omega = 0 \text{ and } \left|T_{fe}\right| < T_{fs} \\ T_{fs} \cdot \operatorname{sgn}(\omega) & \text{if } \omega = 0 \text{ and } \left|T_{fe}\right| \geq T_{fs} \\ T_{fc} + (T_{fs} - T_{fc})e^{\left[-(\omega/\omega_s)^{\delta}\right]} + T_{fv} \cdot \omega & \text{otherwise} \end{cases} \tag{34}$$

where T_{fe} is the driving torque, T_{fs} is the static friction torque, T_{fc} is the Coulomb friction torque, T_{fv} is the viscous friction torque coefficient, ω is the system angular velocity, ω_s is the Stribeck Speed, δ is the Stribeck constant, and sgn() is the symbolic function.

When driving torque T_{fe} is less than static friction torque T_{fs}, the friction torque is equal to the driving torque. When the system is not in motion and the driving torque T_{fe} can overcome the static friction torque T_{fs}, the friction torque becomes a function of static friction torque. When the system is in motion, the friction torque decreases with an increase in angular velocity at low speeds and is presented as

a continuous exponential function related to angular velocity. When the friction torque is outside the exponential function range, it is expressed as a primary function related to the coefficient of viscous friction torque.

An electric caliper is a highly nonlinear mechanically coupled structure, and it is not optimal to analyze the friction model of each module separately, which adds a lot of analytical matching work and causes the model to be too complex and unstable.

In this study, the driving-torque equation of the electric caliper was calculated directly using the target braking torque. An accurate electric caliper friction model was obtained using a parameter identification test.

The braking torque M_B is calculated as:

$$M_B = 2\mu_{bp} F_N R_b \tag{35}$$

M_B can be considered equal to the driving torque T_{fe}, and combined with the formulas in Sections II and III, the clamping force formula can be obtained as follows:

$$F_N = \frac{-4k(n_{p1}\Psi_{f1}I_{s1} + n_{p2}\Psi_{f2}I_{s2})i_g\eta_g\eta_{prsm}\tan\alpha_R}{d_s} \tag{36}$$

Then there is:

$$T_{fe} = \frac{-8k(n_{p1}\Psi_{f1}I_{s1} + n_{p2}\Psi_{f2}I_{s2})i_g\eta_g\eta_{prsm}\tan\alpha_R}{d_s}\mu_{bp}R_b \tag{37}$$

where the controllable quantities are the synthetic current vector magnitudes and I_{s1} and I_{s2} of the two motors.

First, single-motor friction model parameters were identified using an electric caliper prototype. The friction pad was controlled to reach the u_2 position, and the motor was then given a gradually increasing forward voltage by limiting the phase-current amplitude until the motor started to rotate. When the motor was stuck, the test was stopped and the corresponding clamping force was recorded. Next, the phase current amplitude limit was changed and another test cycle was performed until the motor phase current amplitude limit reached its maximum value.

During the test, it was found that the average motor phase current gradually increased before the motor was rotated, until the static friction torque T_{fs} was overcome. When the motor started to rotate, the average value of the motor phase current average value I_{ave} decreased, indicating that the friction torque decreased. Subsequently, as the voltage increased, the motor angular velocity increased and crossed the Stribeck function region, and the motor phase current-averaged value I_{ave} formed a positive relationship with the friction torque until the motor was stuck again.

When performing the motor reversal release test, instead of limiting the phase current amplitude, a preclamping force was applied to the electric caliper before the motor was started. From the moment the motor was started, the voltage ceased to increase. The test was stopped when the friction pad reached the position where gap adjustment was completed. The same phenomenon of friction torque change was observed during the test; only the rate of curve change was different.

The clamping relationship curve between the single motor angular velocity and friction torque for different pre-clamping forces, and the releasing relationship curve between the single motor angular velocity and friction torque for different pre-clamping forces, are shown in Fig. 8. And the caliper clamping and releasing motors rotate in opposite directions, so the following figures set the clamping direction to be positive and the release direction to be negative on the x and y axes.

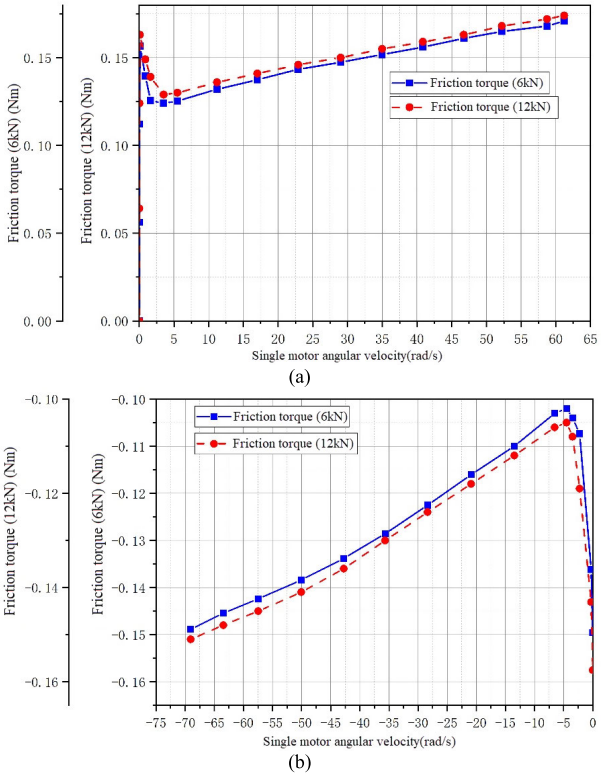

FIGURE 8. Single motor electric caliper friction model fitting curves. (a) The clamping relationship curve between angular velocity and friction torque for different pre-clamping forces. (b) The releasing relationship curve between angular velocity and friction torque for different pre-clamping forces.

The key parameters of the electric caliper friction model for the single-motor operation after parameter identification are listed in Table 7.

TABLE 7. The single motor parameter identification result.

Parameters	Clamping direction	Release direction	Unit
T_{fv}	0.001332	0.000696	$\text{Nms}\cdot\text{rad}^{-1}$
T_{fc}	0.1253	-0.1023	Nm
T_{fs}	0.1632	-0.1496	Nm
ω_s	0.8724	0.6815	$\text{rad}\cdot\text{s}^{-1}$
δ	2	2	--

The response was faster when the two motors were operated simultaneously. The clamping relationship curves between the dual-motor angular velocity and friction torque for different clamping forces and between the dual-motor angular velocity and friction torque for different pre-clamping forces are shown in Fig. 9.

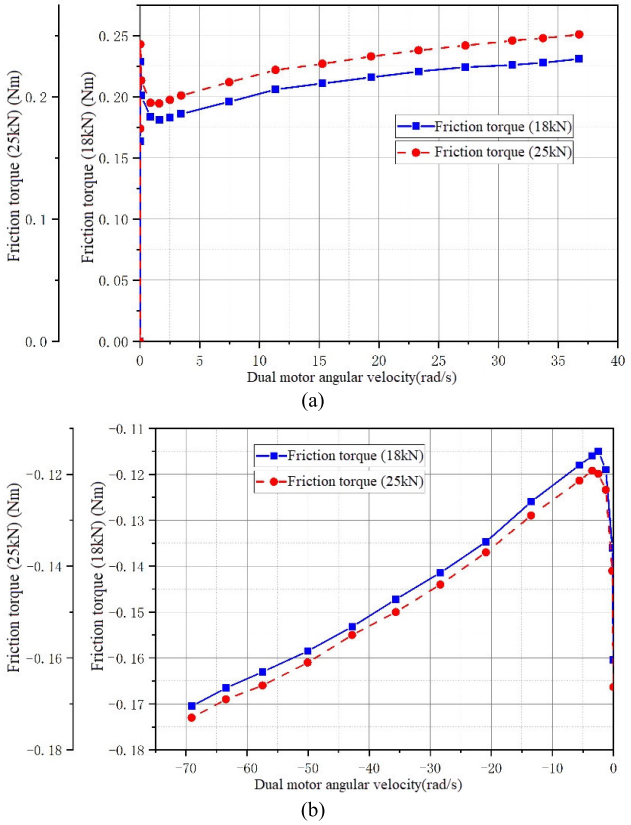

FIGURE 9. Dual-motor electric caliper friction model fitting curves. (a) The clamping relationship curve between angular velocity and friction torque for different pre-clamping forces. (b) The releasing relationship curve between angular velocity and friction torque for different pre-clamping forces.

The key parameters of the electric caliper friction model for the dual-motor operation after parameter identification are listed in Table 8.

TABLE 8. The dual motor parameter identification result.

Parameters	Clamping direction	Release direction	Unit
T_{fv}	0.001576	0.000824	$\mathrm{Nms \cdot rad^{-1}}$
T_{fc}	0.1981	-0.1185	Nm
T_{fs}	0.2431	-0.1663	Nm
ω_s	0.9353	0.7392	$\mathrm{rad \cdot s^{-1}}$
δ	2	2	--

The above parameter identification was performed using the MATLAB System Identification Toolbox. Owing to space constraints, the specific mathematical principles are not listed here [36].

IV. MOTOR WINDING TEMPERATURE ESTIMATION MODEL BASED ON PPO-RL ALGORITHM

Frequent clamping and release of electric calipers cause the temperature of the drive motor to increase. An excessive motor temperature demagnetizes the permanent magnets and increases the motor winding resistance, which in turn affects the proportional relationship between motor output torque and current. Therefore, it is necessary to introduce motor temperature correction to correct the motor output torque.

In this study, we establish a motor-winding temperature model based on the PPO-RL algorithm to predict the motor-winding temperature without temperature sensors. Based on the temperature rise characteristics of the motor winding materials, we analyzed the effect of the motor winding temperature on the motor output torque and performed parameter identification of the motor torque coefficient.

A. PROXIMAL REINFORCEMENT LEARNING STRATEGY

Reinforcement learning (RL) belongs to a class of connectionist learning models. RL focuses on taking appropriate actions based on the environment to maximize the expected reward. The prevailing reinforcement learning algorithms can be classified into three main categories: value-based, policy-based, and actor-critic, where policy-based and value-based algorithms are used to solve the optimal policy and obtain the action that obtains the maximum reward value in each state.

The actor–critic algorithm, which was originally applied in the process of training and controlling the behavior of intelligent body robots, is essentially a class of methods that employs neural internets as estimators of value functions; its general structure is shown in Fig.10.

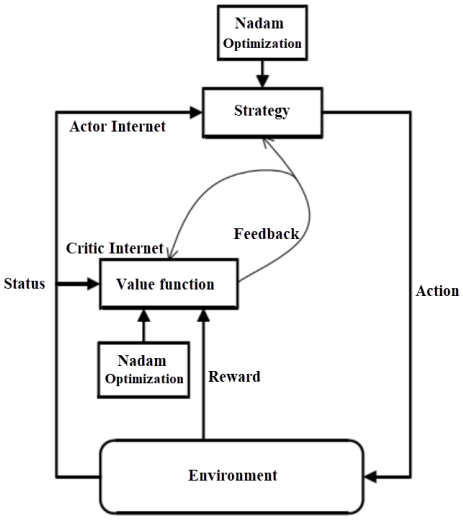

FIGURE 10. Actor-critic reinforcement learning internet.

In this study, we set the state values in an interactive environment as the recorded dataset from the drive motor, and the dynamic selection of the state values was the basis for training the model. The prediction results of the model were provided by the Actor internet. The Critic internet provides a judgment

of the prediction result and feeds the judgment result to the Actor internet through a value function for the gradient update strategy adjustment. Therefore, the feedback from the Critic internet to the Actor internet during the prediction process is particularly important. Gradient optimization of the internet was implemented using the Nadam algorithm, and the reward was the reward value during the training process.

Proximal Policy Optimization (PPO) is a new policy optimization algorithm proposed by OpenAI in 2017, which was initially applied to the control of complex intelligent body robots.

Its advantages are reflected in the supervised process of smart-body training, which can easily achieve training hyperparameter tuning and gradient descent, and recalculate a new updated strategy at each iteration of the training step to minimize the loss function of the training target while ensuring that the strategies produced by two adjacent iterations do not produce large deviations.

The TRPO algorithm is the origin of the PPO algorithm, which was proposed to solve the problem of the inability to ensure monotonically nondecreasing computational performance during gradient descent. The payoff function of the TRPO algorithm is defined as

$$L_\pi(\pi_\theta) = \eta(\pi_{\theta_{old}}) + \hat{E}\left[\frac{\pi_\theta(a_t|s_t)}{\pi_{\theta_{old}}(a_t|s_t)}\hat{A}_t(s_t, a_t)\right] \tag{38}$$

where π_θ is the new strategy, $\pi_{\theta_{old}}$ is the old strategy, $L_\pi(\pi_\theta)$ and $\eta(\pi_{\theta_{old}})$ are the payoff functions of the new and old strategies, respectively, a_t is the action value at moment t, s_t is the state value at moment t, $\hat{E}[]$ function represents the difference between the returns of the new and old strategies.

The implementation of the TRPO algorithm involves finding a replaceable loss function that transforms the solution of the TRPO problem into a solution to the problems in (39) and (40).

$$\underset{\theta}{Max}\ \hat{E}\left[\frac{\pi_\theta(a_t|s_t)}{\pi_{\theta_{old}}(a_t|s_t)}A_t(s_t, a_t)\right] \tag{39}$$

$$subject\ \ to\ \ \hat{E}\left[D_{KL}(\pi_{\theta_{old}}(\cdot|s_t)||\pi_\theta(\cdot|s_t))\right] \le \delta \tag{40}$$

where D_{KL} is the calculated KL dispersion and δ is the threshold value of the average KL dispersion.

The standard computational method of the TRPO algorithm is to approximate the objective function to the first order, expand its constraints to the Taylor second order, and finally solve the optimal parameters using the solution of the conjugate gradient. The above standard computational method leads to a huge computational effort; therefore, OpenAI proposes the use of the first-order gradient of the PPO to solve the above problem. The objective function of the PPO algorithm is given by:

$$L^{CLIP}(\theta) = \hat{E}[Min(r_t(\theta)\hat{A}_t, clip(r_t(\theta), 1-\varepsilon, 1+\varepsilon)\hat{A}_t] \tag{41}$$

where ε is the hyperparameter of the algorithm, $\hat{A}_t$ indicates the advantage of the updated policy, $r_t(\theta)$ is the ratio of the new strategy to the old strategy and is expressed as follows:

$$r_t(\theta) = \frac{\pi_\theta(a_t|s_t)}{\pi_{\theta_{old}}(a_t|s_t)} \tag{42}$$

In this study, the loss error of the actor internet was selected as the objective function of the PPO, and the prediction of motor temperature was achieved by minimizing the objective function.

In the strategy updating process of the prediction method, constraints on the process parameters of the prediction internet are necessary to ensure a high estimation accuracy.

The Nadam algorithm is a class of gradient-updating algorithms that uses Nesterov momentum terms. The advantages include the introduction of a correction $\hat{g}_t$ to the current gradient g_t and the introduction of the mean value $\bar{m}_t$ of the first-order moment estimate m_t to compute the updated gradient $\Delta\theta_t$. This algorithm is described by the following equation:

$$\hat{g}_t = \frac{g_t}{1 - \Pi_{i-1}^t u_i} \tag{43}$$

$$\Delta\theta_t = -\eta\frac{\bar{m}_t}{\sqrt{\hat{n}_t + \xi}} \tag{44}$$

where u_i is the momentum factor of the first-order moment estimate at moment i, η is the Nadam Algorithm Learning Rate, $\hat{n}_t$ is the correction for the second-order moment estimation of gradient at moment t. In summary, the Nadam gradient descent algorithm was used as a constraint on the process parameters of the prediction internet.

B. MOTOR WINDING TEMPERATURE PREDICTION BASED ON PPO-RL ALGORITHM

To predict the motor winding temperature, real motor operating temperature data must first be collected and used for the model algorithm training.

The motor winding temperature measurement method is illustrated in Fig. 11. In this study, a load motor is used to provide the necessary load for the output of the motor gearing mechanism. A rigid connection between the load motor and the motor gear train was achieved using couplings and connecting splines. The power supply supplied the load motor, and the CENTER temperature acquisition device collected the winding temperature of each dual motor.

During the temperature acquisition test, a load of 14 Nm was applied to the load motor based on the external characteristics data, and a long-time operating condition with a dual motor load rate of approximately 70% was simulated to obtain a safety-biased motor winding temperature-rise characteristic curve.

The dual motors operate simultaneously to drive load motor rotation. The motor winding temperature was recorded once every 1 min, and a motor working time and resting waiting time test method that meets the demand of electric caliper characteristics was proposed according to the vehicle braking cycle characteristics. The test flow is shown in Fig. 12, and

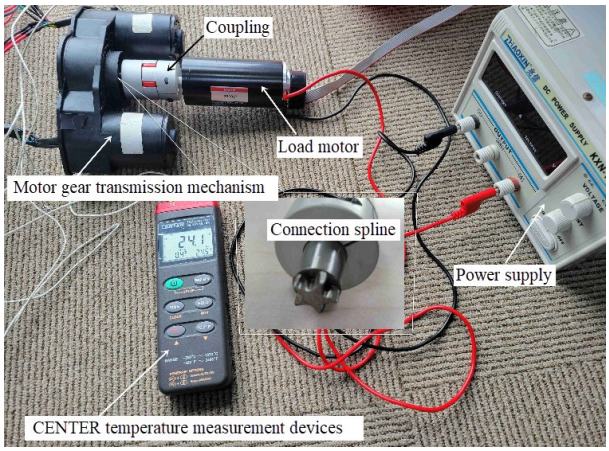

FIGURE 11. Motor winding temperature measurement diagram.

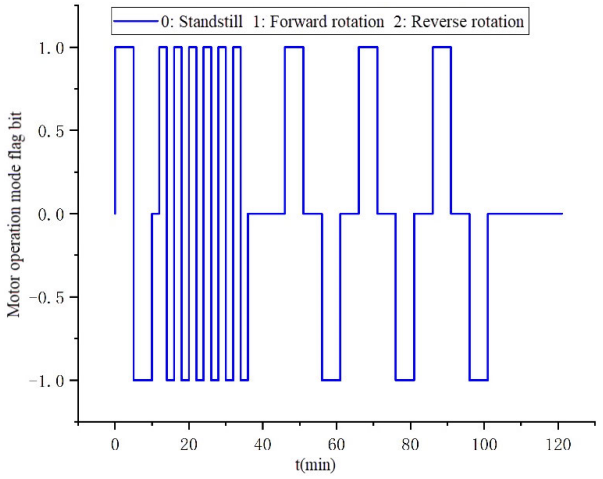

FIGURE 12. Motor operating and resting test cycles.

the average value of the test data from the three test cycles is recorded as the data for the model algorithm training.

The motor winding temperatures of motor 1 and motor 2 are indicated by $Temp_1$ and $Temp_2$, and the mean values of the test data and fitted curves of the three test cycles are shown in Fig. 13.

The structure of the PPO-RL motor winding temperature prediction model algorithm constructed in this study is shown in Fig. 14, in which each Actor and Critic internet contains an input layer, an output layer, and a hidden layer, and the hidden layer uses the ReLU function as the activation function.

In this study, the loss error of the Actor internet was selected as the objective function of the PPO algorithm, and the function of the hidden layer was defined as follows:

$$\begin{bmatrix} h_1 \\ h_2 \\ h_3 \\ h_4 \\ h_5 \\ out_t \end{bmatrix} = \begin{bmatrix} relu(x_t \cdot w_1 + b_1) \\ relu(h_1 \cdot w_2 + b_2) \\ relu(h_2 \cdot w_3 + b_3) \\ relu(h_3 \cdot w_4 + b_4) \\ relu(h_4 \cdot w_5 + b_5) \\ relu(h_5 \cdot w_{out} + b_{out}) \end{bmatrix} \tag{45}$$

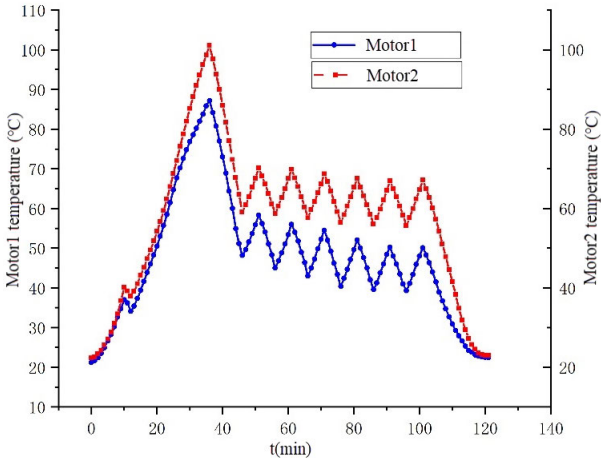

FIGURE 13. Dual-motor winding temperature test.

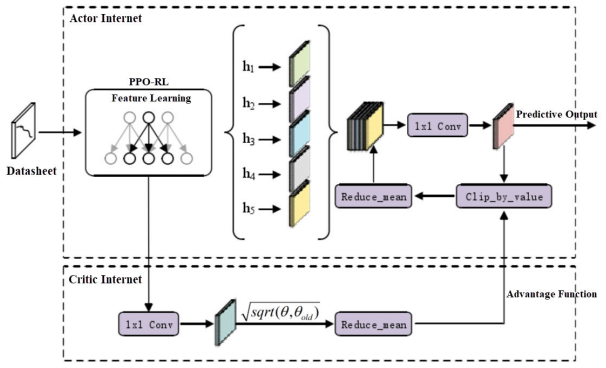

FIGURE 14. PPO-RL temperature prediction model structure.

where x_t is the input data matrix at moment t; w_i, b_i, and h_i represent the respective weights, biases, and outputs of the internet hidden layer; w_{out} and b_{out} represent the weights and biases of the internet output layer, respectively; out_t is the output of the internet at moment t.

In the Critic internet, θ and θ_{old} denote the mapping relationships between the predicted and true target values, respectively, and are used to calculate the dominance value function $\hat{A}_t$, and ratio function $r_t(\theta)$ of the new and old strategies, which are expressed as follows:

$$\hat{A}_t = \frac{1}{N} \sum (out_t - y_t)^2 \tag{46}$$

$$r_t(\theta) = \frac{out_t}{y_t} \tag{47}$$

The dominance value function $\hat{A}_t$ is the mean square error of the predicted output of the Critic internet at time t. The ratio function $r_t(\theta)$ is the ratio between the output out_t of the internet and the real target value y_t. N is the input batch size for each training set. The smaller the absolute value of the dominance value function $\hat{A}_t$, the greater the dominance of the output obtained from the internet prediction to approximate the true data form.

The key parameters of the PPO-RL motor winding temperature prediction model algorithm are listed in Table 9.

TABLE 9. The key parameters of the temperature prediction model.

Parameters	Value
Number of hidden layers	5
Number of hidden layer neurons	(256,128,64,32,16)
Weight initialization	unit normal
Optimizer	Nadam
Learning Rate	$(2 \times 10^{-4}, 1\times 10^{-4})$
Hyperparameter	0.02

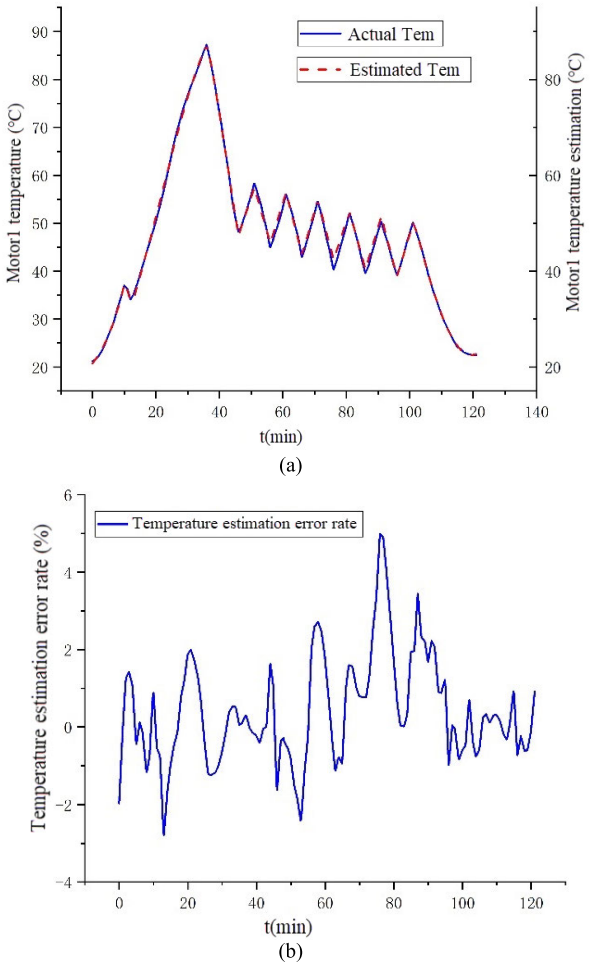

FIGURE 15. (a) Comparison of predicted and real temperature. (b) Temperature estimation error rate.

The data mean fit curve from the test cycle was collated into a data set by sampling every 1 min interval. The dataset was input into the PPO-RL motor winding temperature prediction model to obtain the model prediction data, which were collated with the real data in Fig. 15(a); the error rate is shown in Fig. 15(b). From the results, it can be observed that the prediction results trend of the prediction model is consistent with the real data, with a maximum error rate of 4.98% and an average error rate of 1.06%. Thus, the constructed PPO-RL motor winding temperature prediction model was accurate and reliable.

C. THE EFFECT OF MOTOR WINDING TEMPERATURE ON MOTOR OUTPUT TORQUE

A higher motor winding temperature causes the internal resistance of the motor to increase and the motor output torque to decrease at the same current.

To test the effect of the motor winding temperature on the motor output torque, we first used a temperature box to allow the tested motor to reach the preset temperature $Temp_{tar}$, $Temp_{tar}$ includes five gradients: −25 °C, 0 °C, 23 °C, 40 °C, and 80 °C. Subsequently, the motor supply voltage to 13.5V, different motor stuck currents were set, the motor worked in the stuck state, and the measured value of the torque sensor was recorded. The motor stuck current included 10 gradients, and the data were recorded once every 3A increase. Finally, the correspondence between the motor stuck current and the output torque at different temperatures was obtained, as shown in Fig. 16.

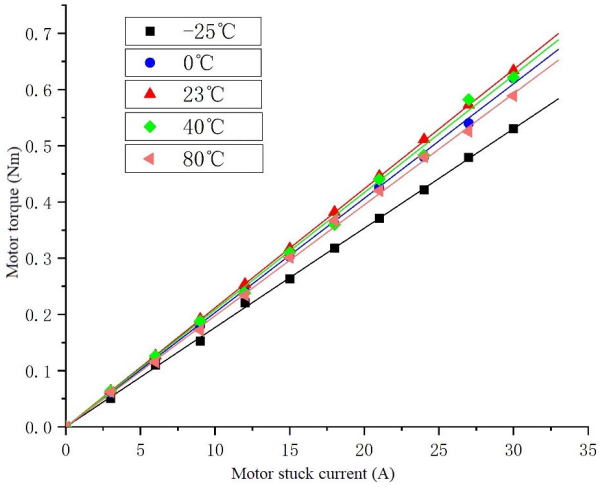

FIGURE 16. The relationship between motor stuck current and output torque at different temperatures.

The curve-fitting of the above data to obtain the motor torque coefficients K_T at different temperatures is presented in Table 10.

TABLE 10. The key parameters of the temperature prediction model.

$Temp_{tar}$/℃	$K_T/Nm \cdot A^{-1}$
-25	0.01768
0	0.02034
23	0.02119
40	0.02085
80	0.01976

In summary, when the motor is stuck, the motor output torque can be obtained using (48) and Table 10, which can be used for the frequent regulation of the clamping force conditions.

$$T_e = f(K_T, Temp_n) \cdot I_s \tag{48}$$

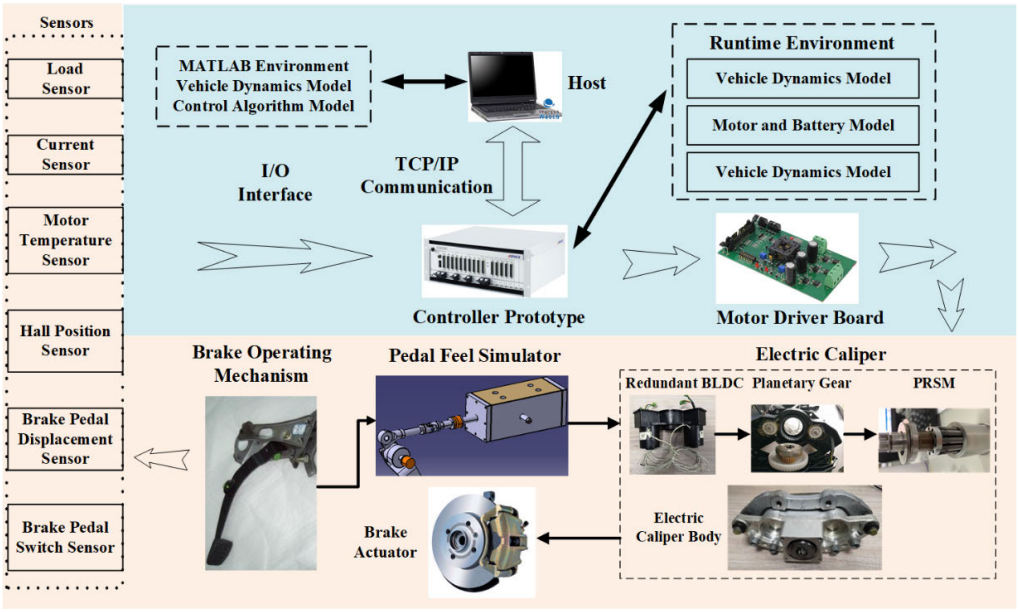

FIGURE 17. Hardware-in-the-loop test bench platform.

V. CLAMPING FORCE ESTIMATION STRATEGY AND HARDWARE-IN-THE-LOOP TEST VERIFICATION

A. STUDY ON CLAMPING FORCE ESTIMATION STRATEGY

In this study, the clamping force distribution is based on the maximum achievable clamping force of a single motor. When the required clamping force $F_{tar} \leq 13kN$, a single motor drive was used, and $F_{tar} > 13kN$, a dual-motor common drive was required.

The strategy for distributing the clamping forces of the two motors under different clamping-force segments is shown in (49). F_{tar1} and F_{tar2} represent the target clamping forces of the two motors.

The advantage is that the life of the motor can be extended, and additionally, mutual redundancy of the two motors can be realized, so that in case of failure of one motor, the other motor can still provide a clamping force of 13 KN, which ensures that the EMB still has the braking capability to meet the regular braking requirements.

$$\begin{cases} \begin{bmatrix} F_{tar1} \\ F_{tar2} \end{bmatrix} = \begin{bmatrix} F_{tar} \\ 0kN \end{bmatrix} & (F_{tar} \leq 13kN) \\ \begin{bmatrix} F_{tar1} \\ F_{tar2} \end{bmatrix} = \begin{bmatrix} 13kN \\ F_{tar} - 13kN \end{bmatrix} & (F_{tar} > 13kN) \end{cases} \tag{49}$$

When the electric caliper enters the clamping state, the electric caliper clamping fine state bits are first analyzed, and then different clamping force estimation strategies are assigned based on different state bits. In this paper, we summarize the following four electric caliper clamping fine-state positions.

a. Brake disc friction pad contact state bit Λ_1: indicates that the brake disc is in contact with the friction pad.

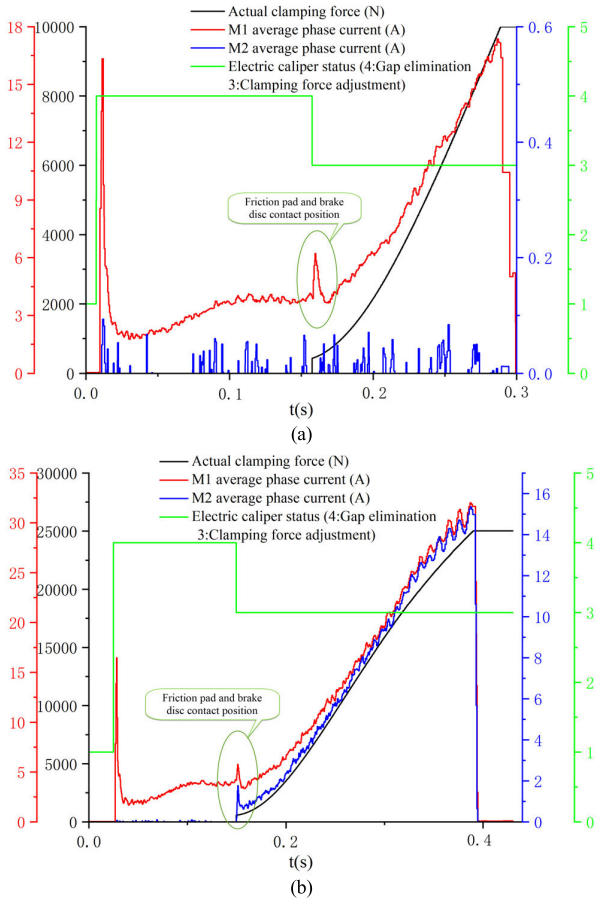

FIGURE 18. Electric caliper response time test. (a) 15kN target clamping force curve. (b) 25kN target clamping force curve.

b. First clamping force climbing completion state bit Λ_2: This indicates that the first clamping force climbing of the electric caliper was complete.

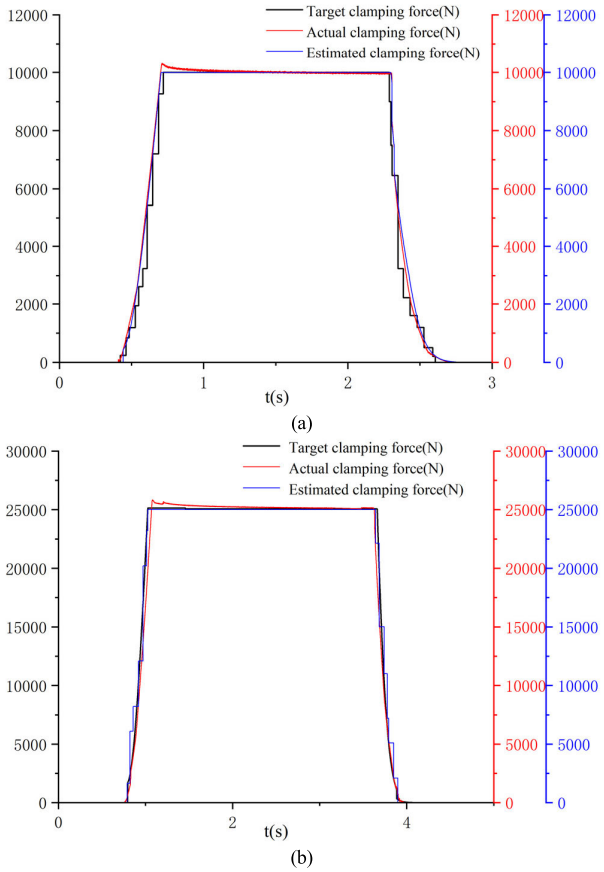

FIGURE 19. First climbing clamping force estimation and following test. (a) 15KN target clamping force curve. (b) 25KN target clamping force curve.

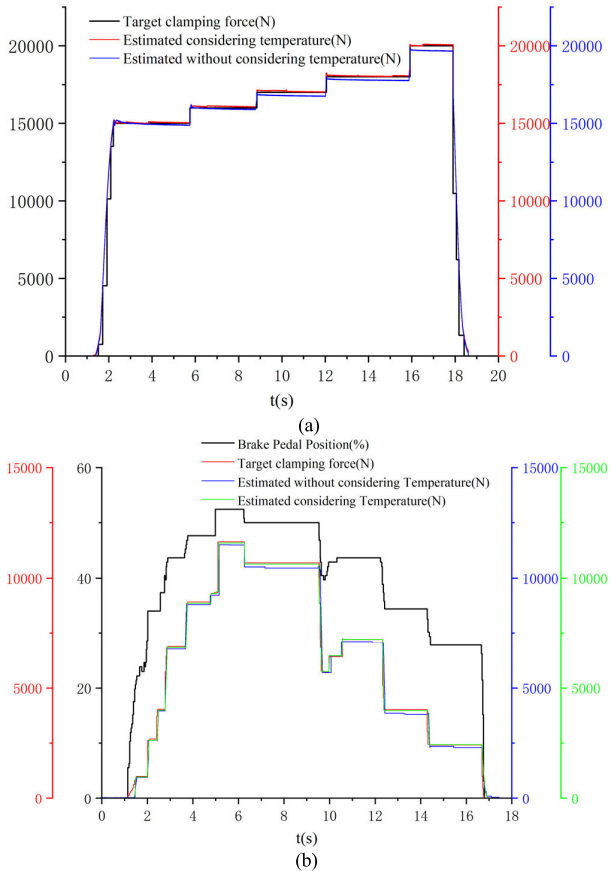

FIGURE 20. Continuously adjustable clamping force estimation and following test. (a) The clamping force up adjustment test curve. (b) Up adjustment error curve.

c. Clamping force up-adjustment state bit Λ_3: This indicates that the electric caliper clamping force is insufficient and must be adjusted upward.

d. Clamping force down state bit Λ_4: indicates that the electric caliper clamping force is too large and needs to be adjusted downward.

To summarize the clamping force estimation strategy as follows:

Strategy 1: From Λ_1 to Λ_2, the clamping force was estimated using an electric caliper stiffness model, which was compensated based on the mean motor phase current.

Strategy 2: From Λ_2 to Λ_3, the clamping force is estimated using the redundant drive electric caliper dynamics equation, which is compensated based on the friction model and the temperature-motor torque parameter model.

Strategy 3: From Λ_3 to Λ_4, the clamping force was estimated using the electric caliper stiffness model.

B. HARDWARE-IN-LOOP BENCH TEST VERIFICATION

An HIL test based on the proposed system is performed to further illustrate the effectiveness of the proposed control strategy.

The HIL test bench platform is shown in Fig. 17.

For the proposed EMB system and clamping force estimation strategy, experiments were conducted to verify the electric caliper response time and continuous following effect, clamping force estimation effect, and continuous up and down adjustment effect, including the clamping force response time and brake pedal continuous input clamping force following the test, the first clamping force climbing test with different target clamping forces, clamping force up and down adjustment tests with or without considering the motor temperature, and single-wheel anti-lock(ABS) function.

Test 1: First, to verify the time-response characteristics of the proposed electric caliper, the target clamping forces were set to 10kN with a single motor operation and 25kN of the maximum clamping force with both motors fully operational.

Refer to Bosch's IPB electro-hydraulic braking system, which has a braking response time of 90-120ms. As shown in Fig. 18 (a)–(b), when the target clamping forces were 10kN and 25kN, the response times were less than 0.3s and 0.4 s, respectively, which are 3 times faster than conventional electro-hydraulic braking systems.

Test 2: In this test, the first clamping force climbing test with different target clamping forces was conducted, including a target clamping force of 10kN with a single working motor and a target clamping force of 25kN with a dual motor.

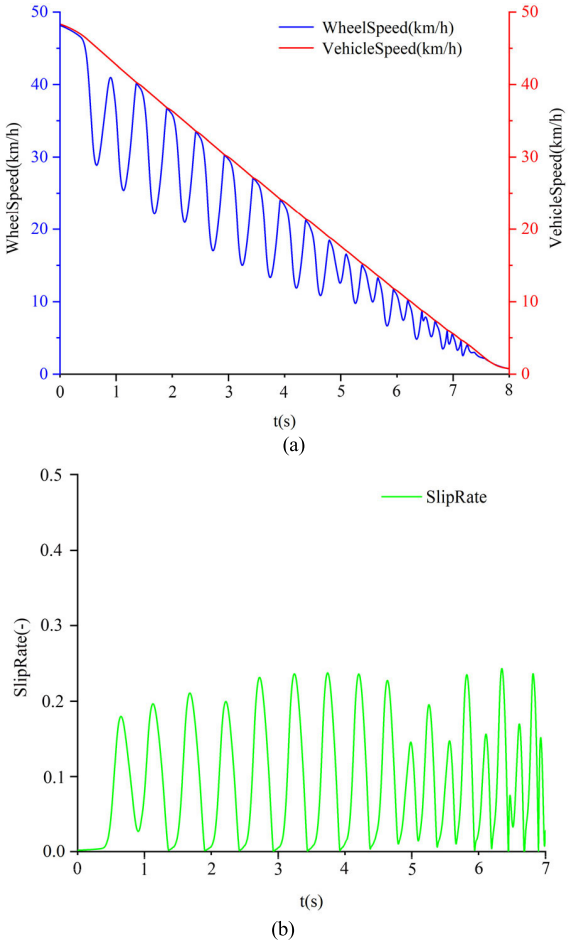

FIGURE 21. Single-wheel ABS function test. (a) The wheel speed and vehicle speed curves. (b) The slip rate curve.

The relationship curves of the estimated clamping force and the actual clamping force with different target clamping forces are shown in Fig. 19(a)–(b). It can be observed that both the estimated clamping force and the actual clamping force exhibit good tracking performance.

Test 3: After the first clamping force climb is completed, when the target clamping force changes, the electric caliper must be frequently adjusted up or down, during which the motor temperature increases.

To verify the influence of the motor temperature on the clamping force estimation accuracy, the clamping force up adjustment and brake pedal continuous input test curves and error curves with and without considering the motor temperature are shown in Fig. 20 (a)–(b).

The results show that if the influence of the motor temperature is not considered, the estimated clamping force error will increase with the frequent operation of the electric caliper. When using the proposed temperature model, the estimated clamping force curve was maintained around the target clamping force curve, thereby proving the validity of the temperature estimation model.

Test 4: The single-wheel ABS test is conducted on the proposed EMB to verify whether it can effectively regulate the slip rate within a safe range. The test scenario is: the initial speed is 48km/h, the adhesion coefficient is 0.2, and triggering ABS function. The test results are shown in Fig. 21 (a)-(b).

The test results show that the proposed EMB can well regulate the wheel speed to follow the vehicle speed when the ABS is triggered on the low attached road, and the slip rate is basically within 20%, which meets the safety requirements.

VI. CONCLUSION

In this study, a full brake-by-wire system for automatic driving, wired-controlled chassis, and clamping force estimation control strategy based on this system is proposed. The main contributions of this study are as follows:

(1) A full brake-by-wired system with a dual-drive motor as a redundant power source and a planetary roller screw as the motion conversion mechanism was proposed for an autopilot and wire-controlled chassis. The parameters were matched, and a prototype was trial-produced.

(2) Aimed at the proposed full brake-by-wired system, a clamping force estimation control strategy that comprehensively considers the electric caliper dynamics, stiffness, friction, and temperature effects.

(3) A temperature estimation model based on the PPO-RL algorithm is proposed, considering the influence of the motor temperature on the output torque.

(4) Finally, HIL tests were conducted, and the test results verified the effectiveness and superiority of the proposed system and control strategy with three times faster response than EHB, good clamping force continuous-following effect, high estimation accuracy throughout the different operating phases of the electric caliper, and the slip rate can be well regulated within a safe range with ABS function.

In future work, the parameter matching and control strategy will be further optimized to fully utilize the hardware system performance and further improve the control accuracy. Further comparative tests with other latest research results on clamp force estimation are planned to further validate the effectiveness of the clamp force estimation strategy proposed in this paper. Additionally, the effect of the electric caliper friction coefficient on the increase in operating temperature will be investigated, and once the testing of a single EMB has been completed, three more EMBs will be produced to test the ABS function and the fault degradation function at the level of the whole vehicle.

REFERENCES

[1] *Taxonomy and Definitions for Terms Related to Driving Automation Systems for on-Road Motor Vehicles*, SAE Int., USA, SAE J-3016, 2018, p. 35. [Online]. Available: https://www.sae.org/standards/content/j3016_201806/

[2] S. Paolo and P. Luca, "An electromechanical brake caliper actuator," ITA Patent WO 20 160 058 67A2, Jul. 3, 2015.

[3] D. G. Sim and C. S. Shin, "Electro-mechanical brake device," U.S. Patent 10 030 727 B2, Jul. 24, 2018.

[4] J. Wang, Y. Zhang, N. Yang, D. Song, and Q. Wang, "Parameters design and braking efficiency analysis of a hydraulic self-energizing wedge disc brake," *Int. J. Precis. Eng. Manuf.*, vol. 18, no. 10, pp. 1409–1418, Oct. 2017.

[5] J. Li, T. Wu, and L. S. Meng, "An electro-mechanical brake for commercial vehicles with clamping force retention function," CN Patent 10 548 0454, Dec. 12, 2019.
[6] G. Liu, S. J. Ma, and X. J. Fu, *Planetary Roller Screws—Transmission Engagement Principle*. Beijing, CN, USA: Science Press, 2019, pp. 1–2.
[7] S. Ma, T. Zhang, G. Liu, and J. He, "Bond graph-based dynamic model of planetary roller screw mechanism with consideration of axial clearance and friction," *Proc. Inst. Mech. Eng., C, J. Mech. Eng. Sci.*, vol. 232, no. 16, pp. 2899–2911, Aug. 2017.
[8] M. Yao, J. Miao, S. Cao, S. Chen, and H. Chai, "The structure design and optimization of electromagnetic-mechanical wedge brake system," *IEEE Access*, vol. 8, pp. 3996–4004, 2020.
[9] T. Wu, J. Li, and X. Qin, "Braking performance oriented multi-objective optimal design of electro-mechanical brake parameters," *PLoS ONE*, vol. 16, no. 5, May 2021, Art. no. e0251714.
[10] O. Topcu, Y. Tascioglu, and E. I. Konukseven, "Design and multi-physics optimization of rotary MRF brakes," *Results Phys.*, vol. 8, pp. 805–818, Mar. 2018.
[11] C. Kim, Y. Kim, O. Kwon, J. Seo, D. Lee, and H. Yi, "An application of the brain limbic system–based control to the electromechanical brake system," *Adv. Mech. Eng.*, vol. 10, no. 2, Feb. 2018, Art. no. 168781401875521.
[12] L. Durali, A. Khajepour, and S. Jeon, "Design and optimization of a cam-actuated electrohydraulic brake system," *Proc. Inst. Mech. Eng., D, J. Automobile Eng.*, vol. 232, no. 7, pp. 909–920, Jun. 2018.
[13] M. Ye and H. Wang, "A robust adaptive chattering-free sliding mode control strategy for automotive electronic throttle system via genetic algorithm," *IEEE Access*, vol. 8, pp. 68–80, 2020.
[14] J. Zhou, J. Gao, K. Wang, and Y. Liao, "Design optimization of a disc brake based on a multi-objective optimization algorithm and analytic hierarchy process method," *Trans. FAMENA*, vol. 42, no. 4, pp. 25–42, Mar. 2019.
[15] J. Kim, C. Jo, Y. Kwon, J. S. Cheon, S. J. Park, G. B. Jeon, and J. Shim, "Electro-mechanical brake for front wheel with back-up braking," *SAE Int. J. Passenger Cars-Mech. Syst.*, vol. 7, no. 4, pp. 1369–1373, Sep. 2014.
[16] C. Jo, S. Hwang, and H. Kim, "Clamping-force control for electromechanical brake," *IEEE Trans. Veh. Technol.*, vol. 59, no. 7, pp. 3205–3212, Sep. 2010.
[17] Y. Zhao, H. Lin, and B. Li, "Sliding-mode clamping force control of electromechanical brake system based on enhanced reaching law," *IEEE Access*, vol. 9, pp. 19506–19515, 2021.
[18] G. Qiao, G. Liu, Z. Shi, Y. Wang, S. Ma, and T. Lim, "Effect of friction torque on electromechanical brake system dynamics," *SAE Int. J. Vehicle Dyn., Stability, NVH*, vol. 1, no. 2, pp. 471–479, Jun. 2017.
[19] C. F. Lee and C. Manzie, "High-bandwidth clamp force control for an electromechanical brake," *SAE Int. J. Passenger Cars-Electron. Electr. Syst.*, vol. 5, no. 2, pp. 590–599, Sep. 2012.
[20] S. Kwon, S. Lee, J. Lee, and D. Kum, "Accurate state estimation for electro-mechanical brake systems," *J. Electr. Eng. Technol.*, vol. 14, no. 2, pp. 889–896, Feb. 2019.
[21] G. Park, S. Choi, and D. Hyun, "Clamping force estimation based on hysteresis modeling for electro-mechanical brakes," *Int. J. Automot. Technol.*, vol. 18, no. 5, pp. 883–890, Oct. 2017.
[22] L. H. Xia, "The study on distributed hybrid braking system based on EMB," Ph.D. dissertation, Automot. Electron., Chongqing Univ., Chongqing, CN, USA, 2019.
[23] S. Saric, A. Bab-Hadiashar, and J. V. D. Walt, "Estimating clamp force for brake-by-wire systems: Thermal considerations," *Mechatronics*, vol. 19, no. 6, pp. 886–895, Sep. 2009.
[24] Y. H. Ki, K. J. Lee, J. S. Cheon, and H. S. Ahn, "Design and implementation of a new clamping force estimator in electro-mechanical brake systems," *Int. J. Automot. Technol.*, vol. 14, no. 5, pp. 739–745, Sep. 2013.
[25] J. Li, T. Wu, T. Fan, Y. He, L. Meng, and Z. Han, "Clamping force control of electro–mechanical brakes based on driver intentions," *PLoS ONE*, vol. 15, no. 9, Sep. 2020, Art. no. e0239608.
[26] R. Hoseinnezhad, A. Bab-Hadiashar, and T. Rocco, "Real-time clamp force measurement in electromechanical brake calipers," *IEEE Trans. Veh. Technol.*, vol. 57, no. 2, pp. 770–777, Mar. 2008.
[27] S. Eum, J. Choi, S.-S. Park, C. Yoo, and K. Nam, "Robust clamping force control of an electro-mechanical brake system for application to commercial city buses," *Energies*, vol. 10, no. 2, p. 220, Feb. 2017.
[28] S.-K. Baek, "A performance evaluation of control method using force sensor compensation of electro-mechanical brake," *J. Korea Academia-Ind. Cooperation Soc.*, vol. 23, no. 12, pp. 1–6, Dec. 2022.
[29] Y. Zhao, H. Lin, H. Elahi, F. Miao, and S. Riaz, "Clamping force sensor fault analysis and fault-tolerant control of the electromechanical brake system," *Arabian J. Sci. Eng.*, vol. 48, no. 5, pp. 6011–6023, May 2023.
[30] M. S. Jneid, M. Zöldy, and P. Harth, "Sensorless optimal control of electronic wedge brake based on dynamic model and Kalman filter state multiple-estimation," *Proc. Inst. Mech. Eng., D, J. Automobile Eng.*, Apr. 2023. [Online]. Available: https://journals.sagepub.com/doi/10.1177/09544070231168168
[31] C. Li, G. Zhuo, C. Tang, L. Xiong, W. Tian, L. Qiao, Y. Cheng, and Y. Duan, "A review of electro-mechanical brake (EMB) system: Structure, control and application," *Sustainability*, vol. 15, no. 5, p. 4514, Mar. 2023.
[32] Y. Li, T. Shim, D.-H. Shin, S. Lee, and S. Jin, "Control system design for electromechanical brake system using novel clamping force model and estimator," *IEEE Trans. Veh. Technol.*, vol. 70, no. 9, pp. 8653–8668, Sep. 2021.
[33] M. Heydrich, V. Ricciardi, V. Ivanov, M. Mazzoni, A. Rossi, J. Buh, and K. Augsburg, "Integrated braking control for electric vehicles with in-wheel propulsion and fully decoupled brake-by-wire system," *Vehicles*, vol. 3, no. 2, pp. 145–161, Mar. 2021.
[34] D. Czerwinski, J. Geca, and K. Kolano, "Machine learning for sensorless temperature estimation of a BLDC motor," *Sensors*, vol. 21, no. 14, p. 4655, Jul. 2021.
[35] H. Shi, S. Hu, and J. Zhang, "LSTM based prediction algorithm and abnormal change detection for temperature in aerospace gyroscope shell," *Int. J. Intell. Comput. Cybern.*, vol. 12, no. 2, pp. 274–291, Jun. 2019.
[36] J. Lin, Z. Niu, X. Zhang, H. Ma, Y. Zhao, and Q. Han, "Clamp nonlinear modeling and hysteresis model parameter identification," *IEEE Access*, vol. 9, pp. 147757–147767, 2021.

LIANG CHU was born in 1967. He received the B.S., M.S., and Ph.D. degrees in automotive engineering from Jilin University, Changchun, China. He is currently a Professor and a Doctoral Supervisor with the College of Automotive Engineering, Jilin University, China. His research interests include driving and braking theory and control technology for new energy vehicles, which include powertrain and brake energy recovery control theory and technology, energy management theory and working condition adaptive technology, and brake-by-wire system and distributed drive-brake integrated control theory and technology for automatic vehicles.

PENGH ZHU was born in 1992. He received the B.S. degree from the College of Automotive Engineering, Jilin University, Changchun, China, in 2015, where he is currently pursuing the Ph.D. degree. His research interests include braking energy recovery technology, brake-by-wire system theory and technology, and assisted driving technology for battery and automatic vehicles.

CHENG CHANG was born in 1997. He received the B.S. degree from the College of Automotive Engineering, Jilin University, Changchun, China, in 2019, where he is currently pursuing the Ph.D. degree. His research interests include braking energy recovery technology, brake-by-wire systems, distributed drive-brake integrated control theory and technology, and assisted driving technology for battery and automatic vehicles.